**Showcasing a study on Li-ion diffusion in Li-excess spinel lithium manganese oxide by Weiji Xiao at School of Advanced Materials, Peking University Shenzhen Graduate School.**

Insight into fast Li diffusion in Li-excess spinel lithium manganese oxide

Ab initio calculations show that Li-excess configuration can enhance Li-ion diffusion in spinel lithium manganese oxide by introducing two kinds of fast diffusion channel with low energy barrier.
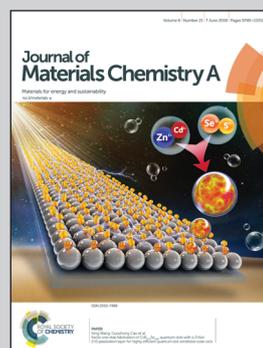
ROYAL SOCIETY OF CHEMISTRY

rsc.li/materials-a

PAPER

Insight into fast Li diffusion in Li-excess spinel lithium manganese oxide†

Weiji Xiao,[a] Chao Xin,[b] Sibai Li, [iD][a] Jianshu Jie,[a] Yue Gu,[a] Jiaxin Zheng,*[a] and Feng Pan [iD] *[a]

Li-excess cathode materials are expected to have great potential for applications in lithium-ion batteries owing to their high energy density. In addition to the extensive studies on the anionic redox activity in lithium-ion batteries, their Li-ion diffusion properties have also attracted much interest. Using *ab initio* calculations, herein, we systematically explored Li diffusion properties in both stoichiometric and Li-excess phases of spinel lithium manganese oxide (LMO). Our results showed that there is a type of structural unit (six Mn ions forming a cation ring for Li-ions to pass through during migration) that acts as "gate sites" and the Li-excess configuration could introduce two types of fast Li-ion migration channels to enhance the Li-ion diffusivity. The first type of fast channels resulted from the decreased repulsive coulombic interactions between the cations at the gate site and the mobile Li-ions due to the substitution of Mn^{3+} by Li^+. The second type of fast channels originated because the excess Li could induce more gate sites with symmetrical distribution of Mn^{4+} surrounding the Li diffusion channel, which is proved to be able to enhance the Li-ion mobility. Interestingly, it was also found that in slow Li diffusion channels for both stoichiometric and Li-excess LMO, a simultaneous polaron hopping process around the gate sites would be coupled with the Li migration process, which accounts for the high energy barriers for Li-ion diffusion.

Introduction

Li-excess cathode materials for rechargeable lithium-ion batteries (LIBs) have attracted tremendous attention.[1–5] In addition to the additional capacity induced by their anionic redox activity, it is also found that the Li-excess phase is beneficial for Li ion transport. Combining experiments and *ab initio* calculations, Park *et al.*[6] demonstrated that the local Li-excess configuration of $Li_{1+x}Fe_{1-x}PO_4$ unlocked the restrictive Li ion diffusion in the olivine structure by providing additional Li diffusion paths. Billaud *et al.*[7] experimentally and theoretically confirmed that the formation of Li-excess $Li_{2+2x}Fe_{1-x}SiO_4$ can enhance the Li ion diffusivity by at least two orders of magnitude in silicate intercalation materials. Using *ab initio* calculations, Shin *et al.*[8] proved that pristine layered Li_2MnO_3 Li-excess material exhibits excellent Li mobility, enabling facile Li extraction from both the transition metal layer and Li layer; thus, they deduced that the observed inferior rate behavior of this class of cathode materials cannot be blamed on intrinsic

bulk ionic mobility. Urban *et al.*[9] applied Monte–Carlo percolation simulations on rocksalt-type lithium metal oxides and found that a critical Li-excess concentration exists, at which the Li-ion percolation occurs to enhance the Li-ion transport. Yet, there is a lack of research on Li-ion diffusivity in spinel Li-excess $Li_{1+x}Mn_{2-x}O_4$ materials, whose structure ensures three-dimensional diffusion paths rather than one- or two-dimensional diffusion for Li-ions in the materials mentioned above.

With its thermal safety, non-toxicity, and low cost, spinel lithium manganese oxide (LMO) has been widely used for cathode materials in LIBs.[10] Fig. 1(a) illustrates the structure of the spinel $LiMn_2O_4$. It crystallizes in the cubic crystal structure of space group $Fd\bar{3}m$ with O ions at the 32e sites, forming a cubic close-packed array. The cation distribution can be described as $(Li)[Mn_2]O_4$, where parentheses () and brackets [] denote tetrahedral and octahedral sites, respectively. The tetrahedral 8a sites are occupied by Li ions, while the octahedral 16d sites are occupied by Mn ions. Among all possible ionic defects in $LiMn_2O_4$, lithium antisite created by replacing some of the Mn ions in the 16d sites with Li ions is dominant,[11] resulting in Li-excess phase $Li_{1+x}Mn_{2-x}O_4$, whose cation distribution is designated by $(Li)[Li_xMn_{2-x}]O_4$. The spinels (Li) $[Li_xMn_{2-x}]O_4$ are equilibrium phases according to phase diagram study reported by Paulsen *et al.*[12] and have been synthesized in various previous studies.[13–16] The remaining half

[a]*School of Advanced Materials, Peking University Shenzhen Graduate School, Shenzhen 518055, China. E-mail: zhengjx@pkusz.edu.cn; panfeng@pkusz.edu.cn*

[b]*School of Science, Changchun University of Science and Technology, Jilin Key Laboratory of Solid-state Laser Technology and Application, Changchun, 130022, China*

This journal is © The Royal Society of Chemistry 2018

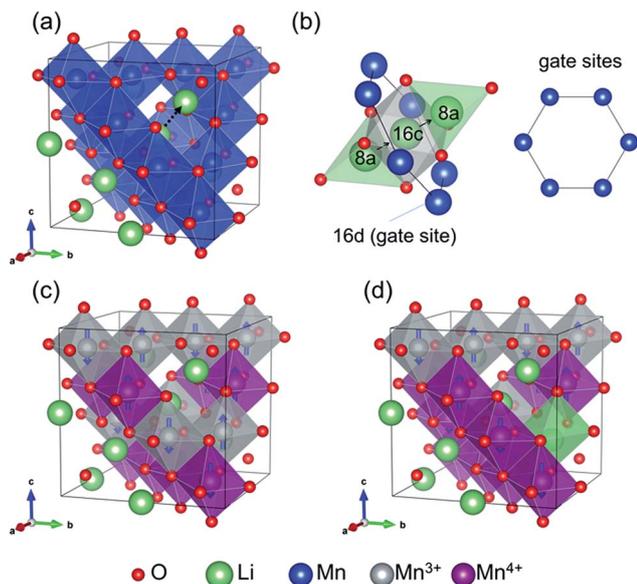*J. Mater. Chem. A*, 2018, **6**, 9893–9898 | 9893

Fig. 1 (a) Crystal structure of spinel $LiMn_2O_4$. Mn ions reside in octahedrons formed by O ions. Dotted arrow denotes a Li diffusion path. (b) Schematic picture of the Li diffusion channel from a tetrahedral 8a site to the adjacent 8a site through an octahedral 16c vacancy surrounded by six Mn ions in octahedral 16d gate sites. (c) and (d) Valence arrangements and magnetic orderings of Mn ions in stoichiometric $Li_8Mn_{16}O_{32}$ and Li-excess $Li_9Mn_{15}O_{32}$, respectively. The arrows across Mn ions denote directions of spin polarization.

of the octahedral cation sites in the structure are 16c vacancies. The 16c vacancy site is thought to serve as a Li migration path that is connected by two adjacent Li ions at the 8a site.[17,18] Each 16c site is surrounded by six 16d sites forming a cation ring in the plane that is perpendicular to the Li diffusion path, which is a type of structure unit that acts as "gate sites" for Li-ions to pass through during migration as shown in Fig. 1(b). Three-dimensional diffusion paths can be formed inside the structure since each face of an 8a site is shared with a 16c site. Therefore, it is reasonable to speculate that LMO can deliver high power in spite of its low theoretical capacity of about 148 mA h g^{-1}. However, pure $LiMn_2O_4$ is found to have an insufficient rate capability.[19] Tateishi *et al.*[17] performed a molecular dynamics study on Li migration in $LiMn_2O_4$ and regarded the Mn atom's e_g orbital electron hopping as the trigger of the Li diffusion mechanism. First-principles calculations applied by Nakayama *et al.*[20] concluded that the valence state of the cations around the Li diffusion path is the dominant factor in determining the migration energy of the Li jump in spinel oxides. Furthermore, Xu *et al.*[18] inferred that higher amount of Mn^{4+} rather than Mn^{3+} may lower the Li diffusion activation barriers in LMO. All these studies were focused on the stoichiometric phase, while the intrinsic Li ion diffusivity in Li-excess LMO has not been studied yet.

Herein, using extensive *ab initio* calculations, we investigated Li-ion diffusivity in spinel lithium manganese oxides $Li_{1+x}Mn_{2-x}O_4$ with $x = 0$ (stoichiometric phase) and $x = 0.125$ (Li-excess phase). Our calculations revealed that Li-excess configuration facilitates the Li-ion mobility by introducing two

types of fast Li-ion migration channels. The first type of fast channels resulted from the decreased repulsive coulombic interactions between the cations at the gate site and the mobile Li-ion due to the substitution of Mn^{3+} by Li^+. The second kind of fast channels originated because the excess Li can induce more gate sites with symmetrical distribution of Mn^{4+} surrounding the Li diffusion channel, which is proved to be able to enhance the Li-ion mobility. Moreover, we also found that in some categories of Li-ion migration channels in both stoichiometric and Li-excess LMO, the Li-ion diffusion was accompanied by a simultaneous polaron hopping process coupled with the Li migration process, which accounted for the high energy barriers for Li-ion diffusion.

Methodology

All the calculations were performed using the Vienna *Ab initio* Simulation Package (VASP)[21,22] based on a generalized gradient approximation with Hubbard U correction (GGA + U)[23,24] to the density functional theory (DFT).[25] The Perdew–Burke–Ernzerhof (PBE)[26] exchange correlation and a plane wave representation for the wave-function with a cut-off of 600 eV were used. The maximum residual force during geometry optimization was less than 0.01 eV Å^{-1} and energies were converged to within 1×10^{-5} eV per atom. The Brillouin zone was sampled by $4 \times 4 \times 4$ special k-points using the Monkhorst–Pack scheme.[27] According to previous studies on Mn-based compounds,[28,29] the Hubbard U value for Mn-d orbitals was set at 4.2 eV. Anti-ferromagnetic (AFM) order was used.[28] The climbing image nudged elastic band (cNEB) method[30,31] was used to investigate the minimum energy pathways of the Li hopping from one lattice site to the adjacent positions. At first, the location of the hopped Li ion and a vacancy at the two potential minima were specified to calculate the initial and end point configurations and the corresponding total energies. Then, intermediate configurations between initial and end points were generated with the linear interpolation method. Finally, the intermediate configurations were optimized under the constraint condition, in which the ions were connected by springs to maintain equal spacing to neighboring configurations. A supercell composed of eight-formula units of $LiMn_2O_4$ (*i.e.* $Li_8Mn_{16}O_{32}$) was used for stoichiometric phase and one lithium antisite was introduced to obtain Li-excess phase $Li_{1.125}Mn_{1.875}O_4$ (*i.e.* $Li_9Mn_{15}O_{32}$). In cNEB calculations, one lithium vacancy for each supercell was set.

Results and discussion

We started with the stoichiometric supercell $Li_8Mn_{16}O_{32}$. Then, the Li-excess supercell $Li_9Mn_{15}O_{32}$ was constructed by substituting one Mn ion at the 16d site with a Li ion. Due to the Li-excess configuration, the ratio of Mn^{3+} to Mn^{4+} changed from 8 : 8 to 5 : 10. Consequently, different behaviors in structure parameters, electronic structures, as well as Li diffusion properties were observed.

Structure parameters of $Li_{1+x}Mn_{2-x}O_4$

After structure optimization, the cubic cells transformed into tetragonally distorted cells. The calculated lattice constants of the stoichiometric supercell $Li_8Mn_{16}O_{32}$ were $a = b = 8.22$ Å and $c = 8.76$ Å, as shown in Table 1, which agreed with the experimental results (8.11 and 8.65 Å).[32] Lattice constants along the z-direction were clearly elongated by about 6.5% compared to that observed in the other two directions. As for the Li-excess supercell $Li_9Mn_{15}O_{32}$, the lattice elongation along the z-direction was of about 4.3% with $a = b = 8.23$ Å and $c = 8.58$ Å (Table 1). The constants for a and b of these two supercells were nearly the same, while the c constant of the stoichiometric supercell was larger than that of the Li-excess supercell. As a result, the Li-excess phase had a smaller cell volume compared to the stoichiometric phase. All these phenomena could be attributed to both the creation of more Mn^{4+} for charge compensation in Li-excess and the Jahn–Teller (JT) effect of Mn^{3+}. As shown in Fig. 2, the bond lengths between Mn^{4+} and O atoms were 1.94 Å and 1.97 Å along the x/y and z directions, respectively, while the bond lengths between Mn^{3+} and O atoms were 1.97–1.98 Å in the xy-plane and 2.19–2.23 Å along the z-direction due to the JT distortion of the $Mn^{3+}O_6$ octahedron. This was the reason for the lattice constant elongation along the z direction. More Mn^{4+} ions in the Li-excess LMO would weaken the JT distortion to the reduction in the difference between the lattice a/b and c. Moreover, as shown in Fig. 2, the average Mn–O bond length of Mn^{4+} was shorter than that of Mn^{3+}, which explains the difference in the volumes of the supercells since there are more Mn^{4+} and less Mn^{3+} ions in the Li-excess phase than in the stoichiometric phase.

Table 1 Calculated structure parameters of stoichiometric $Li_8Mn_{16}O_{32}$ and Li-excess $Li_9Mn_{15}O_{32}$

	a/b (Å)	c (Å)	Volume (Å³)
$Li_8Mn_{16}O_{32}$	8.22(4)	8.76(2)	592.60(1)
$Li_9Mn_{15}O_{32}$	8.23(5)	8.58(8)	582.40(8)

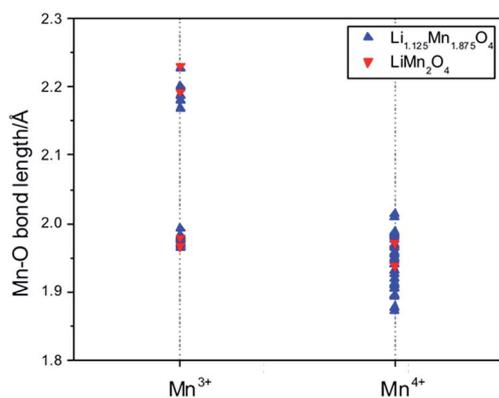**Fig. 2** Mn–O bond lengths of Mn^{3+}/Mn^{4+} in stoichiometric $LiMn_2O_4$ and Li-excess $Li_{1.125}Mn_{1.875}O_4$.

Charge distribution, electronic structure, and magnetic ordering in $Li_{1+x}Mn_{2-x}O_4$

The JT effect in spinel LMO comes from the orbital degeneracy of JT active Mn^{3+} ions, whose electron configuration is $t_{2g}^3e_g^1$.[1] In comparison, the electron configuration of JT inactive Mn^{4+} ion is t_{2g}^3. The charge separation between Mn^{3+} and Mn^{4+} was successfully distinguished by our projected density of states (PDOS) calculation as shown in Fig. 3. The t_{2g} orbitals of both Mn^{3+} and Mn^{4+} ions were fully occupied. The e_g orbitals of Mn^{4+} ion were unoccupied, while the e_g orbitals of Mn^{3+} ion split into two orbitals of occupied d_{z^2} and unoccupied $d_{x^2-y^2}$ states, resulting in larger magnetic moment of Mn^{3+}. According to our calculations, each high-spin Mn^{3+} ion had a magnetic moment of about 3.87 μ_B, while each low-spin Mn^{4+} ion had a magnetic moment of about 3.23 μ_B, which was consistent with previous studies.[28,33] The variation in the Mn^{3+}/Mn^{4+} ratio was also reflected in PDOS, where the density of Mn^{3+} 3d orbital decreased and that of Mn^{4+} increased for the Li-excess phase as shown in Fig. 3(b). Fig. 1(c) shows the valence arrangement and magnetic ordering of Mn ions in $Li_8Mn_{16}O_{32}$. Anti-ferromagnetic (AFM) Mn^{3+} layers ($\uparrow\downarrow\uparrow\downarrow$) and ferromagnetic (FM) Mn^{4+} layers alternate along the [001] direction. This AFM pattern is the same as one of the stable charge orderings of $LiNi_2O_4$[34] and was proved by Liu *et al.*[28] as the most stable configuration in $LiMn_2O_4$ since the 90° Mn^{3+}–O^{2-}–Mn^{3+} in the Mn^{3+}-(001) planes couple *via* the superexchange interaction. In the case of the Li-excess supercell, where the excess Li ion occupies a 16d site as a substitution of Mn ion, various substituted configurations were explored in consideration of valence separation and spin polarization of Mn ions, between which the energy difference was smaller than 0.01 eV; Fig. 1(d) shows the energy favorable configuration. A Mn^{3+} ion was replaced by Li ion and two Mn^{3+} ions in the same (001) planes were oxidized to Mn^{4+} for charge compensation. The AFM pattern remained unchanged after relaxation, while the superexchange interaction ought to have been weakened since the amount of Mn^{3+} decreased. Moreover, magnetic moments of O ions changed with the introduction of excess Li^+ since an electron exchange existed between Mn and O ions. However, the changes of magnetic moments of O ions were smaller than 0.09 μ_B according to our calculations. This could be explained by the fact that 3d electrons of Mn were far more localized than 2p electrons of O. Based on this discussion, it
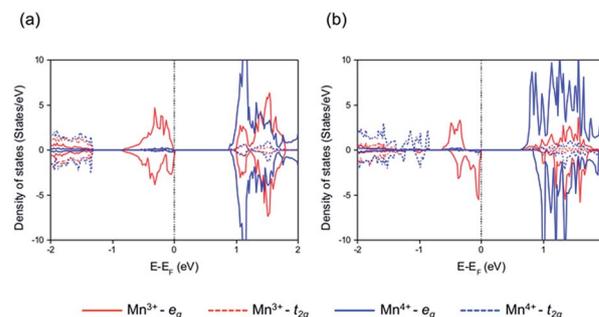

Fig. 3 Projected density of states of Mn-3d in stoichiometric $Li_8Mn_{16}O_{32}$ (a) and Li-excess $Li_9Mn_{15}O_{32}$ (b).

could be concluded that although not specifically, the charge balance was mainly accommodated by Mn ion.

The enhanced Li diffusivity in $Li_{1+x}Mn_{2-x}O_4$

As mentioned above, Li ion jumps through the 16c octahedron, which shares the edges with six octahedral cations in 16d sites. In the following discussion, we will refer to these six edge-sharing sites as gate sites (Fig. 1(b)) since they determine whether a diffusion channel is open or closed. Fig. 4 shows the energy barriers for Li through different diffusion channels and their corresponding cation distributions in the gate sites calculated by the cNEB method. It should be noted that the Mn^{3+}/ Mn^{4+} ratios changed due to the lithium ion removal according to the cNEB calculations. Each supercell contained four Li diffusion paths. According to the gate sites' cation arrangements, two categories were untangled in the stoichiometric supercell (a_1 and a_2) and four in the Li-excess supercell (b_{11}, b_{12}, b_{21} and b_{22}). Based on the locations of the diffusion paths in the supercells, category a_1 was attributed to categories b_{11} and b_{12}, while category a_2 was mapped to categories b_{21} and b_{22}.

In Fig. 4, we can see that in the stoichiometric supercell, a_1 channel shows lower energy barrier (0.38 eV) than a_2 channel (0.72 eV) for Li-ion migration. In the Li-excess supercell, b_{11} and b_{12} show low energy barriers with 0.29 eV and 0.24 eV, respectively, which were significantly lower than that of the a_1 channel in the stoichiometric phase. Thus, the Li-excess configuration introduced two types of fast Li-ion diffusion channels to enhance the Li-ion diffusivity. From the comparison of categories a_1 and b_{11}, it can be seen that substituting Mn^{3+} ion with Li^+ ion led to lower barriers. This was because the coulombic repulsion between the gate site Li^+ (at the 16d site) and the mobile Li^+ was much weaker than that between the original gate site Mn^{3+} and the mobile Li^+. It should be noted that both categories b_{11} and b_{21} had four Mn^{4+} ions, one Mn^{3+} ion, and one Li^+ ion in the gate sites, but b_{11} exhibited lower energy barriers than b_{21}. Compared to category b_{21}, all Mn^{4+} ions in category b_{11} reside in the *para*-positions of the cation ring. As a result, the coulombic repulsive forces formed by the Mn^{4+} ions on the migrating Li^+ ions counteract with each other in a plane perpendicular to the Li diffusion path, which explains the low energy barrier in b_{11}. Compared to b_{11} channel, the six Mn ions at the gate site were all Mn^{4+} in the b_{12} channel, which showed the highest symmetry. Thus, b_{12} channel showed the lowest energy barrier for Li-ion diffusion. The appearance of this fast channel with $(Mn^{4+})_6$ ring gate site could be attributed to the substitution of Mn^{3+} ion with Li^+ ion that leads to the oxidation of Mn^{3+} to Mn^{4+} for charge compensation, which increases the possibility of forming the $(Mn^{4+})_6$ ring gate site. Excess Li^+ would lead to more Mn^{4+} ions in $Li_{1+x}Mn_{2-x}O_4$. Therefore, according to our calculations, fast Li diffusion channels with either more Mn^{4+} or more Li^+ in the gate sites will be created. From this view, the greater the x, the better is the Li diffusion property. However, the crystal structure will become unstable with excess Li^+ ions. According to the phase diagram reported by Paulsen et al.,[12] $Li_{1+x}Mn_{2-x}O_4$ phase remained in equilibrium with $0 < x \leq 1/3$.

Interestingly, the valence states of gate site Mn ions markedly changed during the Li migration in category b_{22}. The transfer of an electron between a pair of two *para* Mn atoms Mn_A and Mn_B occurred by hopping between two equilibrium configurations $Mn_A^{4+}Mn_B^{3+}$ and $Mn_A^{3+}Mn_B^{4+}$ as described in Fig. 5(b). The PDOS of Mn_A transformed from characteristic Mn^{4+} type into Mn^{3+} type, while that of Mn_B showed an opposite trend. This was also confirmed by the change of magnetic
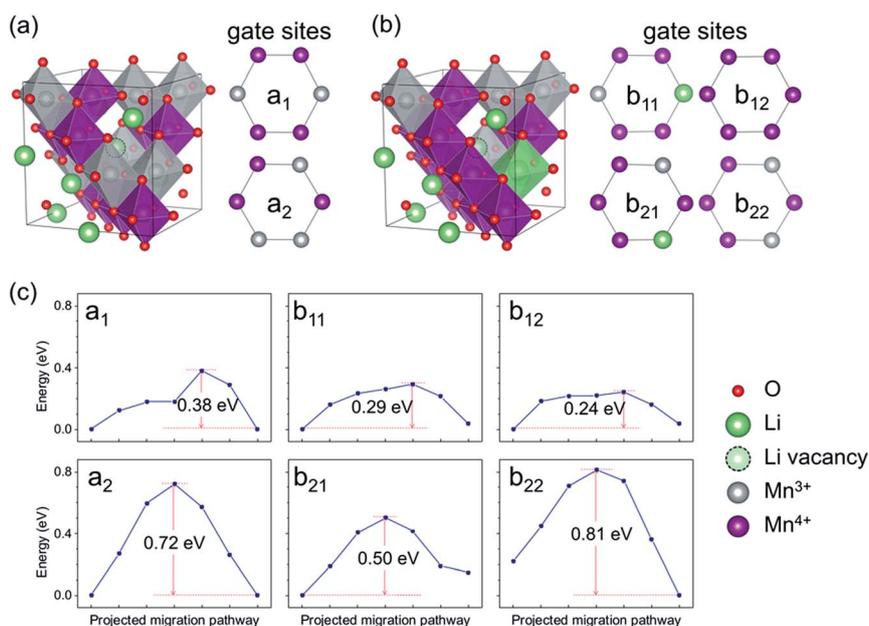

Fig. 4 (a) and (b) Valence arrangements of Mn ions and gate-site cation distributions of different Li diffusion channels in stoichiometric and Li-excess supercells with one Li vacancy, respectively. (c) The energy barriers of different Li diffusion channels with different gate-site cation distributions.
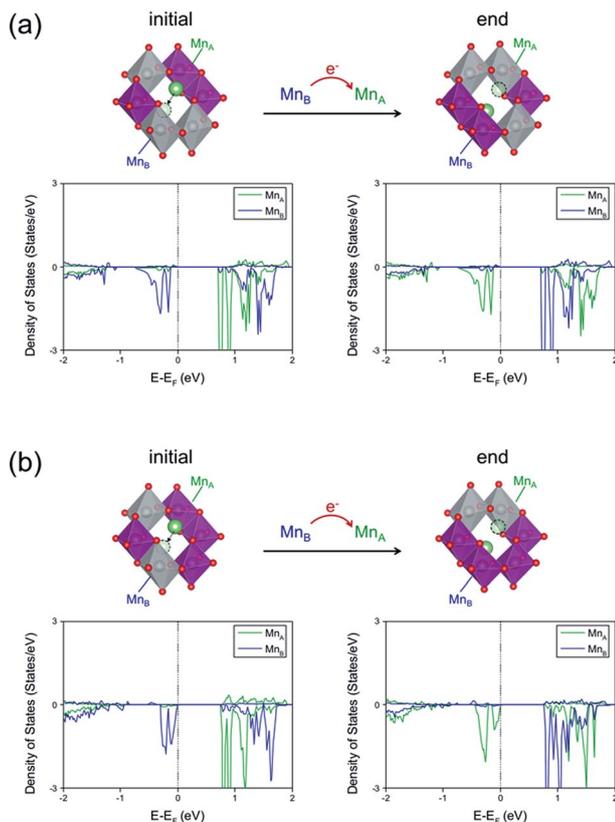
Fig. 5 The gate-site cation distributions along with the projected density of states of two valence-changing Mn ions before and after the Li hopping in Li diffusion channel a_2 (a) and b_{22} (b).

moment: the moment of Mn_A changed from 3.24 μ_B to 3.88 μ_B, and the moment of Mn_B changed from 3.87 μ_B to 3.22 μ_B. This electron transfer process in the cation ring of the gate site could be regarded as a polaron hopping process,[11] which was extensively studied in well-known $LiFePO_4$ cathode materials and other transition metal oxides.[35–40] In the polaron migration process, both the electron (or hole) and its associated local distortion move together, which will be coupled to the Li-ion migration process and in turn would increase the barriers of Li-ion diffusion. This not only explains the high energy barrier in category b_{22}, but also explains the high energy barrier in category a_2 for Li-ion diffusion in stoichiometric LMO, in which the valence states of gate site Mn ions also markedly change with a polaron hopping process during the Li migration as shown in Fig. 5(a). The coupled simultaneous polaron and Li-ion migration processes were also observed in $LiFePO_4$ and were reported to increase the Li-ion diffusion barriers.[35,36] It should be noted that there was also a similar polaron hopping process during Li-ion migration in other channels, but this polaron hopping process did not occur on the gate site Mn_6 ring; thus, it would not affect the Li-ion migration process.

Conclusions

In summary, Li diffusion properties along with charge separation, magnetic orderings, and electronic properties of spinel lithium manganese oxides $Li_{1+x}Mn_{2-x}O_4$ with $x = 0$ (stoichiometric phase) and $x = 0.125$ (Li-excess phase) were investigated systematically. It was found that there was a type of structural unit (six Mn ions forming a cation ring for Li-ions to pass through during migration) to act as "gate sites", and Li-excess configuration in spinel LMO can enhance the Li-ion diffusivity by introducing two kinds of fast Li-ion migration channels. The first type of fast channels resulted from the decreased repulsive Coulomb interactions between the cations at the gate site and the mobile Li-ion due to the substitution of Mn^{3+} by Li^+. Moreover, the excess Li can induce more gate sites with symmetrical distribution of Mn^{4+} surrounding the Li-ion diffusion channel, which resulted in the second type of Li-ion migration channels. Interestingly, in some categories of Li-ion migration channels, Li-ion migration process was accompanied by a simultaneous polaron hopping process, and the coupled effect between them was responsible for the high energy barrier for Li-ion diffusion.

Conflicts of interest

There are no conflicts to declare.

Acknowledgements

Notes and references

1 M. Sathiya, G. Rousse, K. Ramesha, C. P. Laisa, H. Vezin, M. T. Sougrati, M. L. Doublet, D. Foix, D. Gonbeau, W. Walker, A. S. Prakash, M. Ben Hassine, L. Dupont and J. M. Tarascon, *Nat. Mater.*, 2013, **12**, 827.

2 D.-H. Seo, J. Lee, A. Urban, R. Malik, S. Kang and G. Ceder, *Nat. Chem.*, 2016, **8**, 692.

3 P. Rozier and J. M. Tarascon, *J. Electrochem. Soc.*, 2015, **162**, A2490–A2499.

4 P. K. Nayak, E. M. Erickson, F. Schipper, T. R. Penki, N. Munichandraiah, P. Adelhelm, H. Sclar, F. Amalraj, B. Markovsky and D. Aurbach, *Adv. Eng. Mater.*, 2018, **8**, 1702397.

5 R. Shunmugasundaram, R. Senthil Arumugam and J. R. Dahn, *Chem. Mater.*, 2015, **27**, 757–767.

6 K.-Y. Park, I. Park, H. Kim, G. Yoon, H. Gwon, Y. Cho, Y. S. Yun, J.-J. Kim, S. Lee, D. Ahn, Y. Kim, H. Kim, I. Hwang, W.-S. Yoon and K. Kang, *Energy Environ. Sci.*, 2016, **9**, 2902–2915.

7 J. Billaud, C. Eames, N. Tapia-Ruiz, M. R. Roberts, A. J. Naylor, A. R. Armstrong, M. S. Islam and P. G. Bruce, *Adv. Energy Mater.*, 2017, **7**, 1601043.

8 Y. Shin, H. Ding and K. A. Persson, *Chem. Mater.*, 2016, **28**, 2081–2088.

This journal is © The Royal Society of Chemistry 2018

J. Mater. Chem. A, 2018, **6**, 9893–9898 | **9897**

9 A. Urban, J. Lee and G. Ceder, *Adv. Energy Mater.*, 2014, **4**, 1400478.

10 M. M. Thackeray, W. I. F. David, P. G. Bruce and J. B. Goodenough, *Mater. Res. Bull.*, 1983, **18**, 461–472.

11 K. Hoang, *J. Mater. Chem. A*, 2014, **2**, 18271–18280.

12 J. M. Paulsen and J. R. Dahn, *Chem. Mater.*, 1999, **11**, 3065–3079.

13 V. Massarotti, D. Capsoni, M. Bini, G. Chiodelli, C. B. Azzoni, M. C. Mozzati and A. Paleari, *J. Solid State Chem.*, 1999, **147**, 509–515.

14 T. Takada, H. Hayakawa, H. Enoki, E. Akiba, H. Slegr, I. Davidson and J. Murray, *J. Power Sources*, 1999, **81–82**, 505–509.

15 J. Sugiyama, K. Mukai, Y. Ikedo, P. L. Russo, T. Suzuki, I. Watanabe, J. H. Brewer, E. J. Ansaldo, K. H. Chow, K. Ariyoshi and T. Ohzuku, *Phys. Rev. B: Condens. Matter Mater. Phys.*, 2007, **75**, 174424.

16 K. Kamazawa, H. Nozaki, M. Harada, K. Mukai, Y. Ikedo, K. Iida, T. J. Sato, Y. Qiu, M. Tyagi and J. Sugiyama, *Phys. Rev. B: Condens. Matter Mater. Phys.*, 2011, **83**, 094401.

17 K. Tateishi, D. d. Boulay and N. Ishizawa, *Appl. Phys. Lett.*, 2004, **84**, 529–531.

18 B. Xu and S. Meng, *J. Power Sources*, 2010, **195**, 4971–4976.

19 S.-C. Park, Y.-M. Kim, Y.-M. Kang, K.-T. Kim, P. S. Lee and J.-Y. Lee, *J. Power Sources*, 2001, **103**, 86–92.

20 M. Nakayama, M. Kaneko and M. Wakihara, *Phys. Chem. Chem. Phys.*, 2012, **14**, 13963–13970.

21 G. Kresse and J. Furthmüller, *Phys. Rev. B: Condens. Matter Mater. Phys.*, 1996, **54**, 11169–11186.

22 G. Kresse and J. Furthmüller, *Comput. Mater. Sci.*, 1996, **6**, 15–50.

23 J. P. Perdew, J. A. Chevary, S. H. Vosko, K. A. Jackson, M. R. Pederson, D. J. Singh and C. Fiolhais, *Phys. Rev. B: Condens. Matter Mater. Phys.*, 1992, **46**, 6671–6687.

24 A. I. Liechtenstein, V. I. Anisimov and J. Zaanen, *Phys. Rev. B: Condens. Matter Mater. Phys.*, 1995, **52**, R5467–R5470.

25 R. O. Jones and O. Gunnarsson, *Rev. Mod. Phys.*, 1989, **61**, 689–746.

26 J. P. Perdew, K. Burke and M. Ernzerhof, *Phys. Rev. Lett.*, 1996, **77**, 3865–3868.

27 H. J. Monkhorst and J. D. Pack, *Phys. Rev. B: Condens. Matter Mater. Phys.*, 1976, **13**, 5188–5192.

28 W.-W. Liu, D. Wang, Z. Wang, J. Deng, W.-M. Lau and Y. Zhang, *Phys. Chem. Chem. Phys.*, 2017, **19**, 6481–6486.

29 L. Wang, T. Maxisch and G. Ceder, *Chem. Mater.*, 2007, **19**, 543–552.

30 G. Henkelman, B. P. Uberuaga and H. Jónsson, *J. Chem. Phys.*, 2000, **113**, 9901–9904.

31 G. Henkelman and H. Jónsson, *J. Chem. Phys.*, 2000, **113**, 9978–9985.

32 R. Huang, Y. H. Ikuhara, T. Mizoguchi, S. D. Findlay, A. Kuwabara, C. A. J. Fisher, H. Moriwake, H. Oki, T. Hirayama and Y. Ikuhara, *Angew. Chem., Int. Ed.*, 2011, **50**, 3053–3057.

33 C. Y. Ouyang, S. Q. Shi and M. S. Lei, *J. Alloys Compd.*, 2009, **474**, 370–374.

34 A. Kuwabara, C. A. J. Fisher, Y. H. Ikuhara, H. Moriwake, H. Oki and Y. Ikuhara, *RSC Adv.*, 2012, **2**, 12940–12948.

35 Y. Sun, X. Lu, R. Xiao, H. Li and X. Huang, *Chem. Mater.*, 2012, **24**, 4693–4703.

36 T. Maxisch, F. Zhou and G. Ceder, *Phys. Rev. B: Condens. Matter Mater. Phys.*, 2006, **73**, 104301.

37 R. Malik, A. Abdellahi and G. Ceder, *J. Electrochem. Soc.*, 2013, **160**, A3179–A3197.

38 S. Kerisit, K. M. Rosso, Z. Yang and J. Liu, *J. Phys. Chem. C*, 2009, **113**, 20998–21007.

39 H. H. Pham and L.-W. Wang, *Phys. Chem. Chem. Phys.*, 2015, **17**, 541–550.

40 G. Tao, *J. Phys. Chem. C*, 2016, **120**, 6938–6952.